Check for updates

Spirocyclic side chain of a non-fullerene acceptor enables efficient organic solar cells with reduced recombination loss and energetic disorder†

Guangkun Song,‡[a] Yuzhong Huang,‡[b] Fangfang Huang,[b] Xiangjian Wan, [ID] [b] Chenxi Li,[b] Zhaoyang Yao,[b] Yongsheng Chen [ID] *[b] and Yanhui Hou*[a]

Suppressing intramolecular vibration of non-fullerene acceptors (NFAs) by molecular rigidification has been proven to be an effective way to reduce the non-radiative recombination loss and energetic disorder of organic solar cells (OSCs). Thus far, extensive attention has been drawn on rigidifying the fused-ring backbones of NFAs, whereas the highly flexible alkyl side chains are barely concerned. Herein, an effective strategy of side chain rigidification by introducing a spiro-ring is developed for the first time and applied to construct the NFA of **Spiro-F**. Compared to its counterpart **F-2F**, the rigid spirocyclic side chain can constrain the vibrational–rotational motion and control the orientation of two highly flexible *n*-octyl chains effectively. As a result, an optimal molecular packing with enhanced intermolecular actions and lower energetic disorder is achieved by **Spiro-F**, endowing the OSC based on the as cast blend of **PM6:Spiro-F** with a significantly improved PCE of 13.56% and much reduced recombination loss compared to that of **PM6:F-2F**. This work provides a feasible strategy to achieve efficient OSCs through the rigidification of the side chain and could boost the PCEs further if applied to some other efficient systems with smaller bandgaps.

Introduction

Organic solar cells (OSCs) as a green photon-to-current conversion technology have been extensively investigated owing to their excellent merits of light weight, mechanical flexibility, potential low cost *etc.*[1-3] Due to the rapid development of acceptor–donor–acceptor[4] (A–D–A) type non-fullerene acceptors (NFAs), especially the emergence of super-star **Y6** and its analogs, the current certified efficiencies of more than 18% (ref. 5–10) and 20% (ref. 11) have been reached by single-junction and multi-junction OSCs, respectively. In spite of the rapidly increasing PCE of OSCs, there is still a huge efficiency gap between OSCs and perovskite solar cells or inorganic silicon solar cells due to the much higher energy loss (E_{loss}) of OSCs in the charge generation process compared to that of the other two counterparts.[12,13] Note that the best-performing inorganic solar cell displays a very low E_{loss} in gallium arsenide (0.32 eV) and crystalline silicon (0.38 eV),[14] while the record value for perovskite solar cells is 0.34 eV.[15] In sharp contrast, the state-of-the-art OSCs still suffer from a much larger E_{loss} in the range of 0.6–0.9 eV (ref. 16) than that of not only the inorganic or perovskite counterparts, but also the ideal value of 0.25–0.30 eV predicted by Shockley–Queisser (SQ) theory.[17] Therefore, for the sake of further improving PCEs of OSCs, the last but probably most crucial challenge confronted by OSCs should be suppressing E_{loss} to reach comparable open-circuit voltage (V_{OC}) to that of inorganic solar cells with the similar bandgaps (E_g). For instance, if reducing the E_{loss} of OSCs towards similar values 0.4 eV or less to that of PSCs *etc.*, over 20% PCEs could be achieved immediately based on our semi empirical model.[18] Unfortunately, despite the significant progress having been made thus far,[4] it is still unclear in mechanism or lack of effective routes to reduce E_{loss} greatly in OSCs.

Extensive theoretical investigations have indicated that the non-radiative recombination from the lowest-energy charge-transfer (CT) state to ground states (GS) at donor (D)/acceptor (A) interfaces should account for the majority of energy loss in OSCs,[19,20] which is tightly related to the intramolecular vibrations of light-harvesting molecules.[21-24] Moreover, organic semiconductors generally possess the relatively larger energetic disorder than that of inorganic semiconductors, resulting in a substantial broadening of electronic density of states (DOS)[25-27] which is reflected in the absorption of CT states at the

aState Key Laboratory of Separation Membrane and Membrane Processes, Tianjin Municipal Key Laboratory of Advanced Fibers and Energy Storage, School of Materials Science and Engineering, Tiangong University, Tianjin 300387, China. E-mail: houyanhui@tiangong.edu.cn

bState Key Laboratory and Institute of Elemento-Organic Chemistry, The Centre of Nanoscale Science and Technology, Key Laboratory of Functional Polymer Materials, Renewable Energy Conversion and Storage Center (RECAST), College of Chemistry, Nankai University, Tianjin 300071, China. E-mail: yschen99@nankai.edu.cn

† Electronic supplementary information (ESI) available. See DOI: 10.1039/d2ra00253a

‡ Guangkun Song and Yuzhong Huang contributed equally to this work.

D/A interface.[17] Note that the enlargement of energetic disorders, and thus the broadening of DOS could invariably lead to the larger recombination loss including not only the non-radiative but also radiative energy loss.[28–31] The features of CT states are closely related to the components with small bandgap in the D/A blends,[32] indicating that the structure of NFAs is very crucial in reducing energy losses of OSCs due to its dominant role in harvesting low-energy photons. Generally, the state-of-art NFAs usually possess an A–D–A type of molecular architecture, which contributes to not only their superior exciton separation and charge transport, but also the potential to greatly reduce charge generation incurred E_{loss}.[33] Therefore, a lot of structural modifications on NFAs, especially the rigidification of backbones through fused ring strategy to constrain the intramolecular vibrations,[24,34–40] have been explored for mitigating the recombination loss and improving PCEs of OSCs successfully. Note that the highly flexible side chains, *e.g.* alkyl chains, are widely employed in both NFAs and polymeric donors to increase the solubility of materials. However, the resulting severe intramolecular vibrational–rotational motion may cause undesirable molecular packing and more importantly increase the energetic disorders, thus enlarging the recombination loss.[41] Although extensive side chains engineering has been conducted thus far, they are mainly focusing on the length or isomerization of aliphatic chains, where the impact of flexibility has not been investigated.[42–44] Thereby, unveiling the potentially significant effects of side chain flexibility/rigidification on energy losses of OSCs and more importantly, exploring the effective strategies to reduce energy losses should be highly demanded in the studies of OSCs. Note that the above issue still confronts great challenges in terms of molecular design/

synthesis and very few attentions have been drawn on that so far.

In this work, an effective strategy of side chain rigidification by introducing spiro-ring structure is developed for the first time and applied to our previously reported NFA of **F-2F**[45] to construct the target **Spiro-F** (Fig. 1a). As a result, the spirocyclic side chain on **Spiro-F** reduces its degree of freedom for vibrational–rotational motion and tunes its orientation, leading to a red-shifted film absorption, further enhanced intermolecular packing and more importantly reduced energetic disorder with respect to those of the control molecule **F-2F**. When blending with a well-known polymer donor **PM6**, the OSCs employing **Spiro-F** as the acceptor achieves an impressive PCE of 13.56% compared with 12.67% of the control molecule **F-2F** based OSCs, along with an overall ungraded J_{sc} and FF. What is more important, a significantly suppressed E_{loss} was achieved for **Spiro-F** based OSCs with respect to that of **F-2F**, demonstrating the effectiveness of side chain rigidification as a feasible strategy to reduce E_{loss} of OSCs.

The synthetic route to **Spiro-F** was shown in Scheme 1 and the detailed procedures and characterizations were presented in the (ESI†). 2,3-Dimethylbuta-1,3-diene (**1**) was firstly reacted with *n*-BuLi and *t*-BuOK at room temperature and following by addition of 1-bromoheptane to afford compound **2** in a good yield (86%). Then compound **2** underwent a borohydride oxidation at the present of B_2H_6 and H_2O_2 to generate compound **3**, in which the two hydroxy groups were subsequently protected by OTs-groups through reacting with tosyl chloride to yield compound **4** with an excellent yield of 91%. Compound **4** was further dissolved in acetonitrile and reacted with lithium bromide to give 9,10-bis(bromomethyl)octadecane **5** (yield: 74%). Then at the present of KOH, 2,7-dibromo-9*H*-
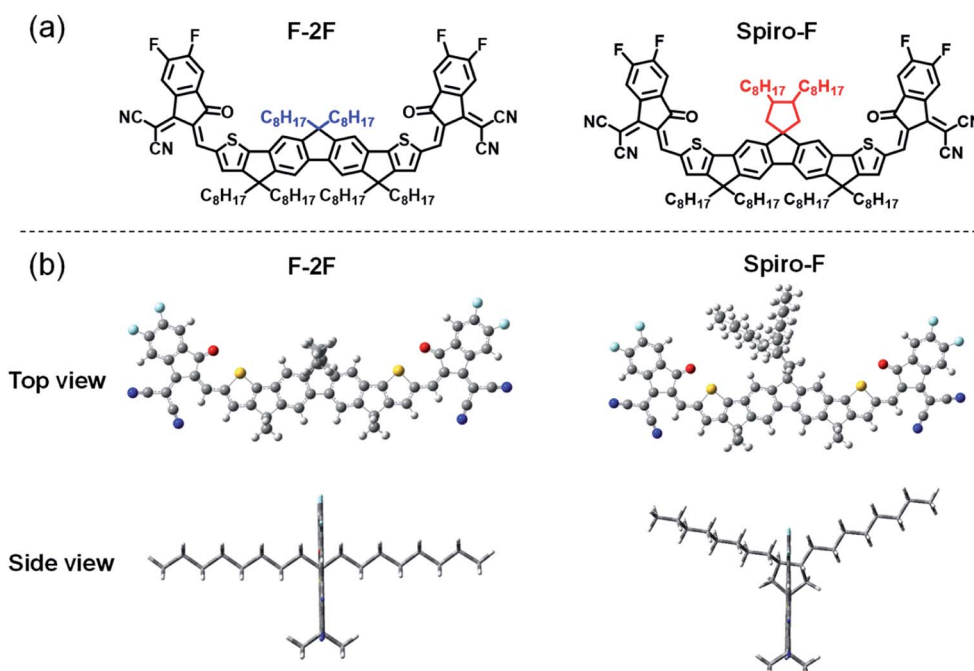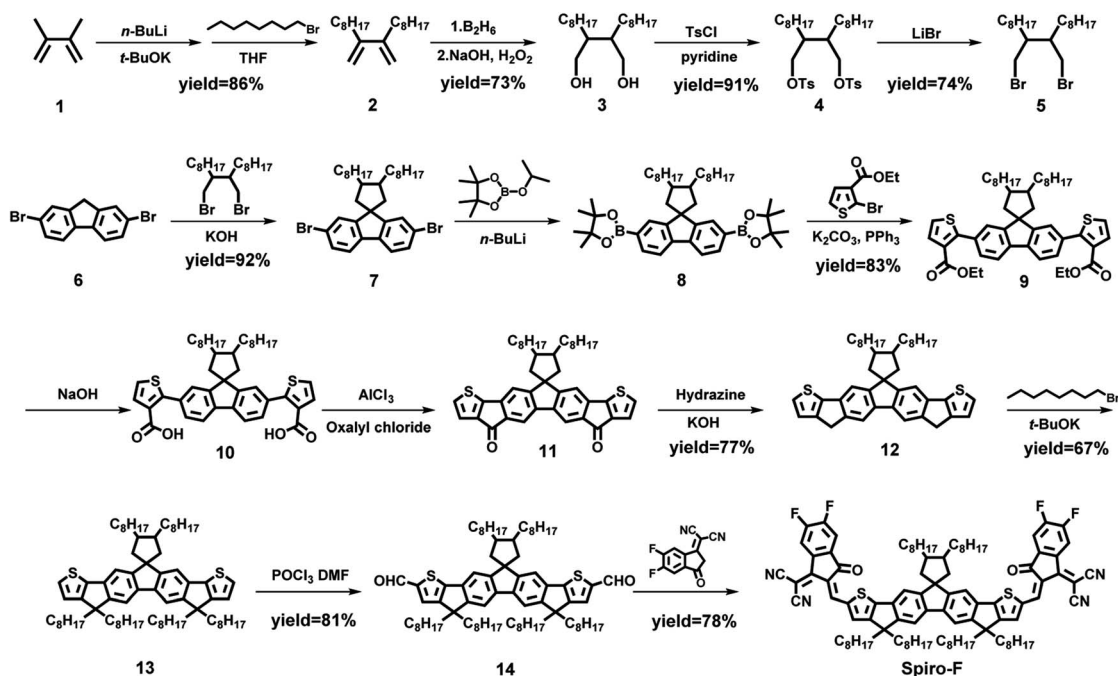

Fig. 1 The chemical structures and optimized geometries of (a) F-2F and (b) Spiro-F from top view and side view.

Scheme 1 The synthetic route to **Spiro-F**.

fluorene (**6**) was performed a very high yield (92%) alkylation using compound **5** as the alkylating regent to obtain compound **7**. Furthermore, compound **7** underwent a halogen–lithium exchange with *n*-butyllithium at a cryogenic temperature and then transformed to its correlated boric acid ester (**8**), which was reacted with ethyl 2-bromothiophene-3-carboxylate directly *via* the Suzuki cross-coupling to afford compound **9** in an overall yield of 83%. Later, compound **9** was hydrolyzed with NaOH as the catalyst, and the hydrolysate was thoroughly acidified with an aqueous hydrochloric acid (1 M) to give compound **10** almost quantitatively. Thereafter, an intramolecular Friedel–Crafts acylation of compound **10** with oxalyl chloride was carried out with the catalysis of acidic AlCl$_3$ to generate the diketone compound **11**, which was further transformed into compound **12** by a reduction using hydrazine. Then the alkylation of compound **12** using 1-bromooctane as the alkylating regent was conducted to afford compound **13** with a moderate yield of 67%, which was further converted into its corresponding dialdehyde (**14**) *via* the Vilsmeier–Haack reaction. Eventually, the target A–D–A type NFA **Spiro-F** was afforded with a decent yield of 78% through a condensation reaction between above dialdehyde and 2-(5,6-difluoro-3-oxo-2,3-dihydro-1*H*-inden-1-ylidene) malononitrile. The chemical structures of key intermediates and target **Spiro-F** were characterized and confirmed by ^{1}H and ^{13}C NMR spectra (Fig. S8–S18 in ESI†), and high-resolution mass spectrometry (Fig. S18 in ESI†). Note that **Spiro-F** exhibited good solubility in widely used organic solvents, such as dichloromethane, chloroform and chlorobenzene, in favor of its solution-processing during the device fabrication.

Fig. 1a displayed the chemical structures of **F-2F** and **Spiro-F**. Note that both NFAs possess the same fluorene based conjugated backbones, enabling spirocyclic side chain the only

difference, so that the side chain effects on energy levels, absorptions, molecular packing, film morphology, even PCEs of OSCs can be clearly investigated below. Density functional theory (DFT) calculations at single molecular level were firstly performed to evaluate the variation of frontier molecular orbital energy levels after introducing the spirocyclic side chain. As it can be expected, both the distributions of frontier molecular orbitals and the corresponding energy levels are not affected by spirocyclic side chain due to the unconjugated property of spiro-rings, thus affording the same highest occupied molecular orbitals (HOMOs) of −5.65 eV and lowest unoccupied molecular orbitals (LUMOs) of −3.45 eV for both **F-2F** and **Spiro-F** (Fig. S1†). However, the plane of introduced spiro-ring is perpendicular to the fluorene backbone as observed obviously from the geometry of **Spiro-F** (Fig. 1b), restricting the orientation of two *n*-octyl groups. This constraint molecular conformation may result in more ordered and tighter intermolecular packing of **Spiro-F** than that of **F-2F**, which should be beneficial to better carrier transportation, lower energetic disorders, smaller recombination loss, and eventually higher PCE of OSCs.

In order to investigate the absorption change of NFAs after substituting by spirocyclic side chain, UV-Vis spectra of **F-2F** and **Spiro-F** in diluted chloroform solutions and nest films were recorded in Fig. 2a. Both **F-2F** and **Spiro-F** possess almost the identical absorption with the maximum absorption peaks λ_{max}^{sol} at 677 and 678 nm, respectively, which can be expected from the same energy levels and bandgaps predicted by the DFT calculation at single molecular level. Note that the greatly red-shifted maximum absorption peaks λ_{max}^{film} can be observed for both **F-2F** and **Spiro-F** from solutions to solid films, indicating the strong intermolecular interactions.[46,47] What is more interesting, the as cast solid film of **Spiro-F** displays the λ_{max}^{film} at
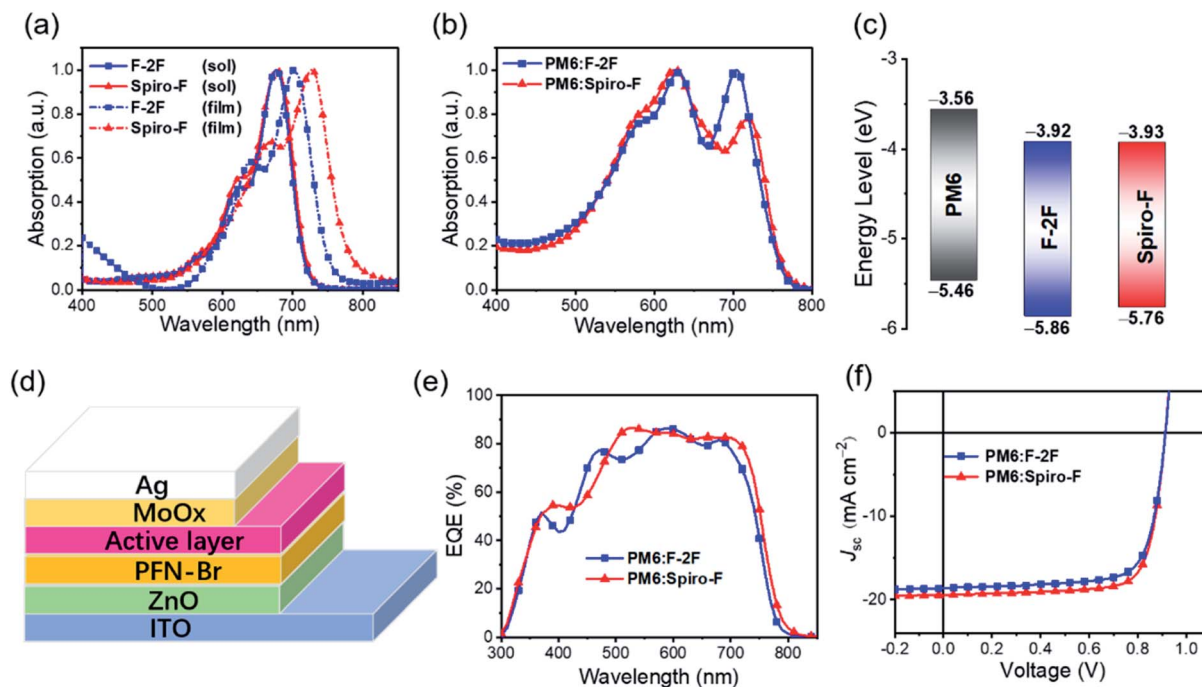
Fig. 2 (a) Normalized absorption spectra of **F-2F** and **Spiro-F** in diluted solutions of chloroform and neat films. (b) Normalized absorption spectra of **PM6:F-2F** and **PM6:Spiro-F** based blend films. (c) Energy level diagram of **PM6**, **F-2F** and **Spiro-F** derived from the electrochemical cyclic voltammetry. (d) The OSC with an architecture of ITO/ZnO/PFN-Br/active layer/MoO$_x$/Ag. (e) EQE curves and (f) current density–voltage (J–V) of the optimized devices.

727 nm, bathochromically shifted by nearly 27 nm comparing to that of 700 nm for **F-2F**, suggesting the enhanced intermolecular π–π stacking of **Spiro-F** with a rigid spirocyclic side chain.[48] Furthermore, the absorption edge (λ_{onset}) of **Spiro-F** is located at 799 nm, also significantly redshifted with respect to that of 773 nm for **F-2F**, corresponding to the optical bandgaps of 1.55 and 1.60 eV, respectively. Note that the polymeric donor **PM6**[49] has been selected as the best to blend with **F-2F** according to our previous work,[45] therefore we further measured the absorption of blend films of **PM6:F-2F** and **PM6:Spiro-F** (Fig. 2b). As it can be observed that both NFAs show the complementary absorption with **PM6**, rendering an efficient light harvesting in a broad range of 500–800 nm.

The experimental energy levels of **F-2F** and **Spiro-F** in solid states were investigated by electrochemical cyclic voltammetry (CV) measurements (Fig. S2†). As shown in Fig. 2c, the similar LUMO energy levels of −3.93 eV and −3.92 eV can be observed by **Spiro-F** and **F-2F**, respectively. However, the HOMO energy level of **Spiro-F** can be estimated at −5.76 eV, having a nearly 0.1 eV unshifting comparing to that of −5.86 eV for **F-2F**.

Therefore, the energy gap of **Spiro-F** could be calculated as 1.83 eV, smaller than that of 1.94 eV for **F-2F**, which is in good accordance with the redshifted absorption of **Spiro-F** film. The detailed parameters for optical absorption and energy levels were listed in Table 1 for a clear comparison.

To evaluate the photovoltaic properties of the two acceptors, bulk heterojunction OSCs with a device structure of ITO/ZnO/PFN-Br/active layer/MoO$_x$/Ag (Fig. 2d) were fabricated. In the device optimization, polymer **PM6** was used as the donor, in considering its well complementary absorption and matched energy levels with both **F-2F** and **Spiro-F**. The detailed data of device optimization were listed in Tables S1 and S2 in ESI.† Fig. 2e displayed the external quantum efficiencies (EQEs) of **F-2F** and **Spiro-F** based OSCs. Among them, over 80% EQE can be achieved in a broad range of 490–725 nm for **Spiro-F** based OSCs, indicating the efficient photon harvesting, exciton dissociation, charge transport and collection. Therefore, the **Spiro-F** based OSCs afford a much larger integrated J_{sc} of 18.89 mA cm^{-2} than that of 17.96 mA cm^{-2} for **F-2F**, in good accordance with the redshifted absorption of **Spiro-F**.

Table 1 Optical properties and electronic energy levels of **F-2F** and **Spiro-F**

Comp.	λ_{max}^{sol} [nm]	λ_{max}^{film} [nm]	HOMO [eV]	LUMO [eV]	E_g^{CVa} [eV]	λ_{onset} [nm]	E_g^{optb} [eV]
F-2F	677	700	−5.86	−3.92	1.94	773	1.60
Spiro-F	678	727	−5.76	−3.93	1.83	799	1.55

^{a} The energy gap derived from CVs. ^{b} The optical bandgap estimated from the absorption onset.

Table 2 Photovoltaic performance parameters of OSCs based on **PM6:F-2F** and **PM6:Spiro-F** measured under the illumination of AM 1.5G (100 mW cm^{-2})

Devices	V_{OC} [V]	J_{sc} [mA cm^{-2}]	FF [%]	PCE [%]
PM6:F-2F	0.913 (0.913 ± 0.02)[a]	18.63 (18.27 ± 0.29)	74.49 (75.30 ± 0.63)	12.67 (12.55 ± 0.19)
PM6:Spiro-F	0.912 (0.909 ± 0.03)	19.45 (19.37 ± 0.28)	76.35 (75.69 ± 0.69)	13.56 (13.31 ± 0.19)

[a] The values in parenthesis are average parameters obtained from 10 devices.

Fig. 2f recorded the current density–voltage (J–V) curves of OSCs based on **F-2F** and **Spiro-F**. For a clear comparison, the related photovoltaic parameters of OSCs were summarized in Table 2. The OSC based on **PM6:F-2F** blend exhibits a good PCE of 12.67% with a V_{OC} of 0.913 V, short-circuit current density (J_{sc}) of 18.63 mA cm^{-2} and fill factor (FF) of 74.49%, which is comparable to that reported in our previous work.[45] After replacing the two n-octyl groups on fluorene of **F-2F** with a spirocyclic alkyl chains, it is worth noting that the OSC based on **PM6:Spiro-F** blend exhibits an impressive PCE of 13.56% with a comparable V_{OC} of 0.912 V. However, both upgraded J_{sc} of 19.45 mA cm^{-2} and FF of 76.35% with respect to that of **PM6:F-2F** based OSCs. In comparison with the OSCs based on **F-2F**, the enlarged J_{sc} of **Spiro-F** should be mainly ascribed to the redshifted absorption, which agrees well with the integrated J_{sc} from the EQE spectrum. The improved FF of **Spiro-F** based device should be attributed to the spirocyclic alkyl chains, which can result in the tighter intermolecular packing,

improved and well-balanced charge mobilities discussed below. The greatly improved PCE of **Spiro-F** based OSCs indicates the effectiveness of introducing rigid spirocyclic alkyl chains to boost the efficiency of OSCs.

In order to reveal the origin of improved J_{sc} and FF for **Spiro-F** based OSCs, the exciton dissociation efficiencies (P_{diss}) were firstly evaluated by measuring the photocurrent densities (J_{ph}) versus effective voltages (V_{eff}) plots for the optimized devices (Fig. 3a). The J_{ph} is obtained from the formula of $J_{ph} = J_L - J_D$, where J_L and J_D are the current densities under illumination and in the dark, respectively. V_{eff} is defined as $V_0 - V$, where V_0 is the voltage when J_{ph} is zero and V is the applied voltage.[50] It is supposed that all photogenerated excitons would be dissociated into free carriers at $V_{eff} = 2$ V where the photocurrent reaches saturation condition (J_{sat}). Therefore, the J_{ph}/J_{sat} ratio can be used to characterize the exciton dissociation and charge collection efficiency. Under short circuit conditions, the J_{ph}/J_{sat} values for **F-2F** and **Spiro-F** based OSCs are 97% and 96%,
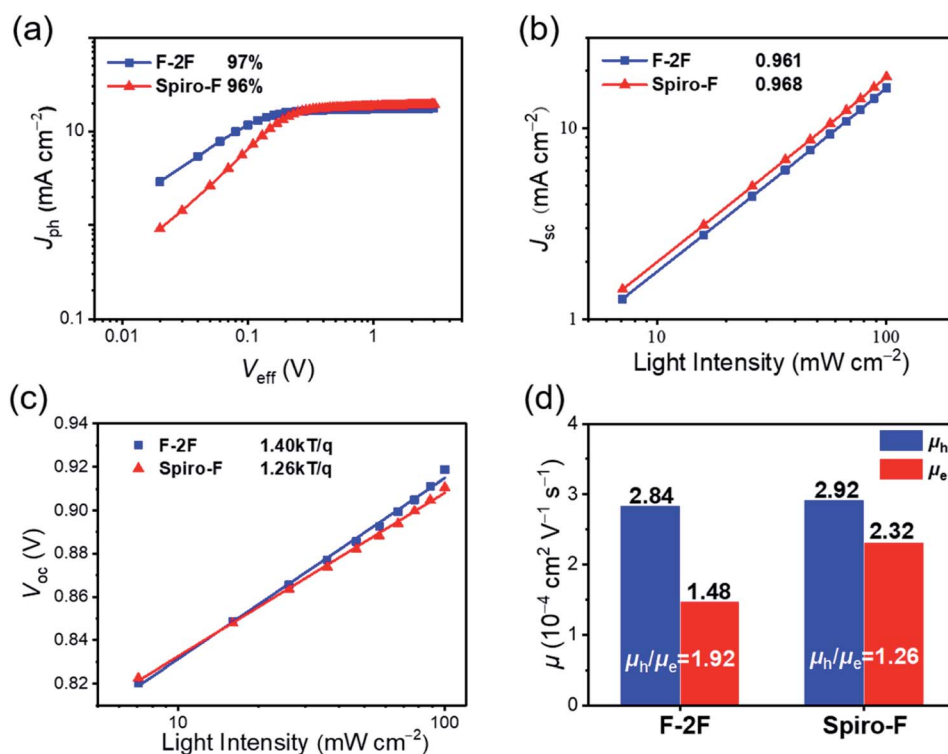
Fig. 3 (a) J_{ph} versus V_{eff} plots. (b) Light intensity (P) dependence of J_{sc} and (c) light intensity (P) dependence of V_{OC} plots for the optimized **PM6:F-2F** and **PM6:Spiro-F** based OSCs. (d) The hole (μ_h) and electron (μ_e) mobilities of **PM6:F-2F** and **PM6:Spiro-F** devices.

respectively, indicating the highly efficient exciton dissociation in both devices. Furthermore, the dependence of J_{sc} on the light intensity (P) has been performed to investigate the bimolecular recombination of OSCs[51] (Fig. 3b). The relationship between J_{sc} and P follows the equation of $J_{sc} \propto P^{\alpha}$, and the bimolecular recombination can be regarded as negligible when α is close to unit.[51] As shown in Fig. 3b, the α values of the optimized **PM6:F-2F** and **PM6:Spiro-F** devices are 0.961 and 0.968, respectively. The indicative negligible charge recombination will be in favor of the high V_{OC} and FFs for both devices. Thereafter, Fig. 3c recorded the V_{OC} dependence of light intensity (P) for the optimized OSCs to evaluate the trap-assist recombination. The slopes (S) of V_{OC} *versus* the natural logarithm of P were calculated to be 1.40 and 1.26 kT/q for **PM6:F-2F** and **PM6:Spiro-F** based OSCs, respectively. The smaller slope for **PM6:Spiro-F** based OSCs indicates the lower trap-assisted recombination loss,[52] which can be further confirmed by its lower energetic disorders below.

The dynamics of free charge were further investigated by employing transient photocurrent (TPC) and transient photovoltage (TPV) measurements in Fig. S3,† respectively, to unveil the carrier transport chrematistics in **PM6:F-2F** and **PM6:Spiro-F** blends. Among them, TPCs were measured at the short circuit condition and can reveal the charge extraction process of OSCs.[53] As displayed in Fig. S3a,† the **PM6:Spiro-F** device demonstrates a faster charge extraction (0.99 μs) comparing to that of **PM6:F-2F** device (1.03 μs), which is beneficial for the charge transport in blend films[45] and also in good agreement with the improved charge mobility of **PM6:Spiro-F** device

discussed below. On the other hand, the TPV measurement could disclose the charge recombination kinetics in OSCs.[54] As shown in Fig. S3b,† the **PM6:Spiro-F** device possesses a longer carrier lifetime of 52 μs than that of 38 μs for **PM6:F-2F** device, indicating a suppressed charge recombination in **PM6:Spiro-F** based OSCs.[55] Moreover, the charge carrier transport ability including the electron mobility (μ_e) and hole mobility (μ_h) of the blended films were estimated by the space-charge limited current (SCLC) method[56] (Fig. S4 and S5†). As shown in Fig. S4,† the electron mobilities of the neat films for **F-2F** and **Spiro-F** are 1.51 and 2.25 $cm^2\ V^{-1}\ s^{-1}$, respectively. The slightly increased electron mobility of **Spiro-F** should be attributed to its rigid spirocyclic side chain. As displayed in Fig. 3d, the **PM6:F-2F** based device exhibits a hole and electron mobility of 2.84×10^{-4} and $1.48 \times 10^{-4}\ cm^2\ V^{-1}\ s^{-1}$, respectively, rendering a μ_h/μ_e ratio of 1.92. Note that for the **PM6:Spiro-F** based device, a similar hole mobility of $2.92 \times 10^{-4}\ cm^2\ V^{-1}\ s^{-1}$, but much larger electron mobility of $2.32 \times 10^{-4}\ cm^2\ V^{-1}\ s^{-1}$ can be achieved with respect to that of **PM6:F-2F**, resulting in a more balanced μ_h/μ_e ratio of 1.26. Apparently, the higher and more balanced charge mobilities for the **PM6:Spiro-F** blend may be caused by the more ordered molecular packing of **Spiro-F** with a rigid spirocyclic alkyl side chain, and should account for the improved FF of **Spiro-F** based device. Note that all the parameters discussed above have been summarized in Table S3† for a clear presentation.

The introduction of rigid spirocyclic alkyl chain on **Spiro-F** will inevitably result in the variation of microscopic morphology of the active layer, which should play a dominant role in the
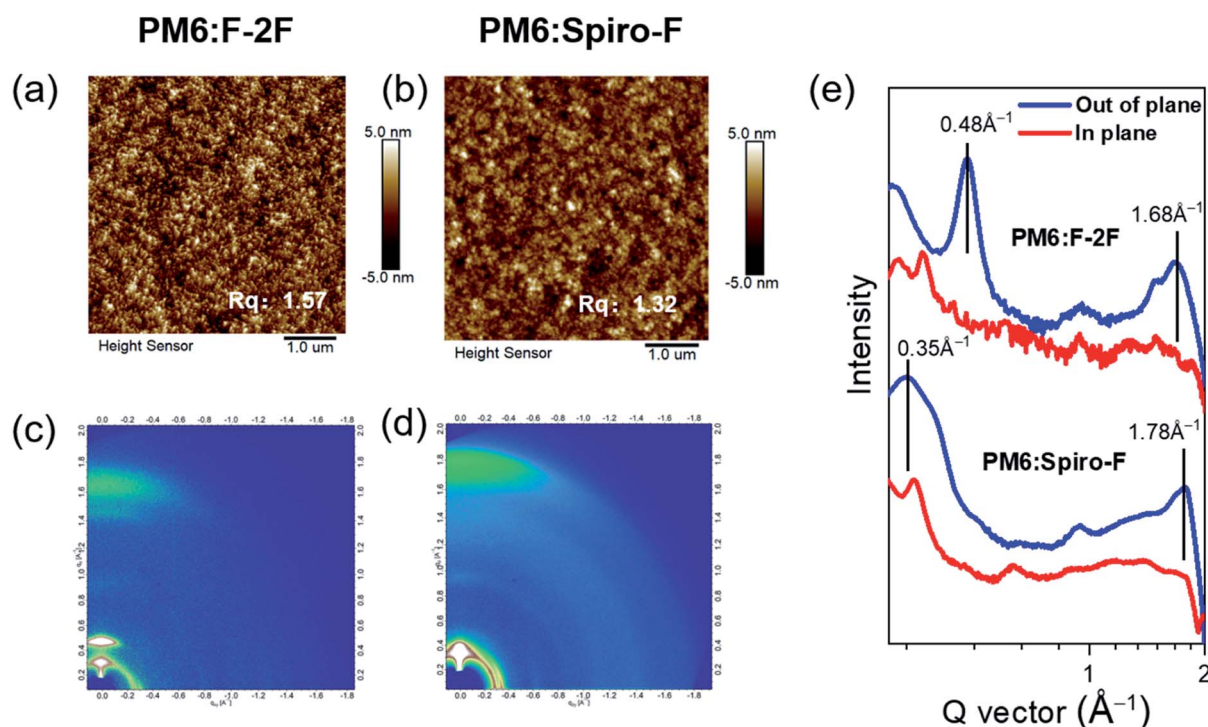

Fig. 4 AFM images for (a) **PM6:F-2F** blend film and (b) **PM6:Spiro-F** blend film. Two dimensional GIWAXS patterns for (c) **PM6:F-2F** blend and (d) **PM6:Spiro-F** blend. (e) In-plane (red lines) and out-of-plane (blue lines) line cuts of the corresponding GIWAXS patterns.

improved J_{sc}, FF and thus PCE for **Spiro-F** based OSCs discussed above. Therefore, it is crucial to unveil the morphology change of active layers from **PM6:F-2F** to **PM6:Spiro-F** at a level of nanoscale. Fig. 4a and b exhibited the images of atomic force microscope (AFM) for **PM6:F-2F** and **PM6:Spiro-F** blends, respectively. The relatively smooth surface can be observed by both **PM6:F-2F** and **PM6:Spiro-F** blends with a root-mean-square (RMS) roughness of 1.57 and 1.32 nm, respectively, due to the good miscibility of **PM6** with both **F-2F** and **Spiro-F**. The smooth surface morphologies in both blended films will be beneficial for the effective contact between active layer and electrode, and thus efficient interfacial charge transfer.

The introduction of a rigid spirocyclic alkyl side chain on central fluorene unit of **Spiro-F** should affect the intermolecular packing markedly, thereby the grazing incidence wide-angle X-ray diffraction (GIWAXS) was further carried out to study the molecular packing and orientation in blended films of **PM6:F-2F** and **PM6:Spiro-F**. Fig. 4c and d displayed the two dimensional GIWAXS patterns for **PM6:F-2F** and **PM6:Spiro-F** blends, respectively. The derived in-plane and out-of-plane line cuts were exhibited in Fig. 4e and the detailed parameters were summarized in Table 3. Note that both blended films possess the preferential face-on orientation as evidenced by the strong (010) $\pi-\pi$ stacking peaks at ~1.7 Å^{-1} in the out-of-plane direction. When taking a more in-depth observation, we found that the **PM6:Spiro-F** film demonstrates a (010) $\pi-\pi$ stacking peak at 1.78 Å^{-1}, corresponding to a distance of 3.52 Å. This is smaller than that of 3.75 Å for **PM6:F-2F** film indicated by the (010) $\pi-\pi$ stacking peak at 1.68 Å^{-1}. Moreover, the crystal coherence length (CCL) in the (010) region for **PM6:Spiro-F** blend can be estimated as 32.9 Å, much larger than that of 20.8 Å for **PM6:F-2F** blend. The enhanced CCL of **PM6:Spiro-F** indicates the more ordered molecular packing,[39] in good accordance with the improved hole/electron mobilities comparing to that of **PM6:F-2F**. Generally, the rigid spirocyclic alkyl side chain in **Spiro-F** constraints the vibrational–rotational motion and controls the orientation of two highly flexible n-octyl chains, in favour of the preferred face-on orientation, ordered and enhanced molecular $\pi-\pi$ stacking and increased CCL. The above superior characteristics of **Spiro-F** facilitate the efficient charge transport and suppressed charge carrier recombination, accounting for the better photovoltaic performance of **PM6:Spiro-F** based OSCs comparing to that of **PM6:F-2F** based one.

As we discussed above, the rigid spirocyclic alkyl side chain on **Spiro-F** could facilitate more ordered and enhanced molecular π–π stacking, thus suppress the recombination loss in OSCs.
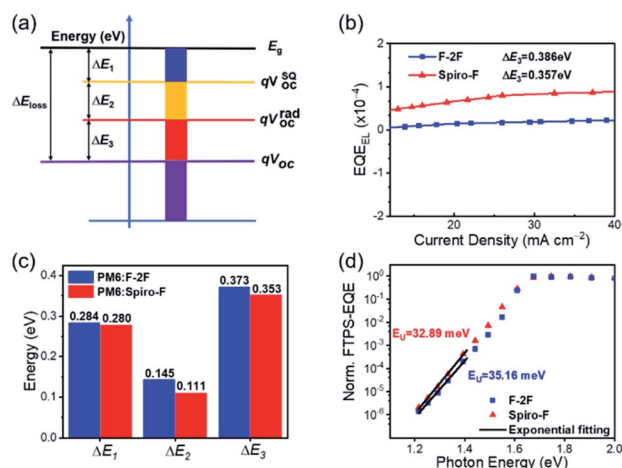

Fig. 5 (a) The total energy losses analysis in OSCs. (b) EQE$_{EL}$ of the devices based on the as-cast **PM6:F-2F** and **PM6:Spiro-F** blended films. (c) Radiative and non-radiative energy losses in the OSCs studied here. (d) FTPS-EQE of the **PM6:F-2F** and **PM6:Spiro-F** based devices at the absorption onset.

Therefore, we analysed the energy losses of OSCs based on both **PM6:F-2F** and **PM6:Spiro-F** blends to disclose the inner relationship of structure-energy loss. The total E_{loss} in OSCs can be categorized into three contributions ($\Delta E_{loss} = \Delta E_1 + \Delta E_2 + \Delta E_3$) based on the detailed balance theory[58] (Fig. 5a): (1) ΔE_1 ($= E_g - qV_{OC}^{SQ}$) is the energy offset between the bandgap edge (E_g) and qV_{OC} in the Shockley–Queisser (SQ) limit (qV_{OC}^{SQ}); (2) ΔE_2 ($= qV_{OC}^{SQ} - qV_{OC}^{rad}$) is the energy offset between the qV_{OC}^{SQ} and qV_{OC} in the radiative limit (qV_{OC}^{rad}); (3) ΔE_3 ($= qV_{OC}^{rad} - qV_{OC}$) is the energy offset between the qV_{OC}^{rad} and qV_{OC} in a realistic OPV devices. As shown in Fig. S6,† the E_g can be accurately determined by the crossing point of normalized absorption and photoluminescence (PL) spectra, being 1.715 and 1.656 eV for **PM6:F-2F** and **PM6:Spiro-F** blends, respectively. Thereby the total E_{loss} can be calculated as 0.802 and 0.744 eV for **PM6:F-2F** and **PM6:Spiro-F** based OSCs, respectively, demonstrating a 0.058 eV reduction after the spiro cyclization of alkyl chains. Among them, the ΔE_1 is the inevitable loss in any types of solar cells[58] and can be calculated to be the nearly identical values of 0.284 and 0.280 eV for **PM6:F-2F** and **PM6:Spiro-F** based OSCs, respectively. The ΔE_2 can be regarded as the additional radiative recombination loss from absorption below the bandgap,[59] which are 0.145 and 0.111 eV for **PM6:F-2F** and **PM6:Spiro-F** based OSCs, respectively. The ΔE_3 is non-radiative energy loss, which usually contributes to the largest part of E_{loss}. Herein, the ΔE_3 for **PM6:Spiro-F** based OSCs is

Table 3 Summary of the GIWAXS parameters for **PM6:F-2F** and **PM6:Spiro-F** films

Blends	q^a (010, Å^{-1})	d^b (010, Å)	FWHM^c (010, Å^{-1})	CCL^d (010, Å)	q (100, Å^{-1})	d (100, Å)
PM6:F-2F	1.68	3.75	0.27	20.8	0.48	13.09
PM6:Spiro-F	1.78	3.52	0.17	32.9	0.33	19.04

^{a} The location of diffraction peaks. ^{b} The π–π stacking distance. ^{c} The full width at half maxima of peaks. ^{d} The crystal coherence lengths calculated from the Scherrer equation: CCL $= 2\pi k$/FWHM.[57]

Table 4 Measured energy losses for **PM6:F-2F** and **PM6:Spiro-F** based devices

Devices	E_g [eV]	V_{OC}^{SQ} [V]	ΔE_1 [eV]	V_{OC}^{rad}	ΔE_2 [eV]	ΔE_3 [eV]	qV_{OC} [eV]	$\Delta E_3{}^a$ [eV]	E_{loss} [V]
PM6:F-2F	1.715	1.431	0.284	1.286	0.145	0.373	0.913	0.386	0.802
PM6:Spiro-F	1.656	1.376	0.280	1.265	0.111	0.353	0.912	0.357	0.744

^{a} The derived non-radiative energy loss from EQE$_{EL}$.

0.353 eV, smaller than that of 0.373 eV for **PM6:F-2F** based ones. The detailed calculation of three parts energy losses above were described in ESI.† Moreover, the reduced ΔE_3 of **PM6:Spiro-F** based OSCs is also confirmed by the much higher external electroluminescence quantum efficiency (EQE$_{EL}$) of devices in Fig. 5b, based on the equation: $\Delta E_3 = -k_B T \ln(\text{EQE}_{EL})$,[60] where k_B is Boltzmann's constant and T is absolute temperature. As shown in Fig. S7,† we have measured the PL and PL quenching yields (PLQY) of **F-2F** and **Spiro-F** films. The PLQY of **F-2F** and **Spiro-F** films are 0.87% and 1.07%, respectively. The increased PLQY for **Spiro-F** film with respect to that of **F-2F** could reduce the non-radiative decay, which should be in favor of the smaller ΔE_3 for corresponding OSCs.[20] Note that low photon energy losses or recombination losses achieved by the **PM6:Spiro-F** device is mainly a combined result of both reduced ΔE_2 and ΔE_3 (Table 4).

As discussed in recent dedicated studies,[29,30,61,62] the absorption edge broadening effects[63] (reflecting the ΔE_2) and the non-radiative recombination loss (ΔE_3) are closely correlated to the energetic disorder which is determined by the microscopic properties of blended films. For an organic semiconductor, the relatively larger energetic disorder than that of the inorganic semiconductor is generally observed, accounting for a substantial broadening of the electronic density of states (DOS) of light-harvesting materials.[25–27] The broadening of the DOS invariably thrusts tail states further into the bandgap, resulting in the large recombination losses in OSCs.[28] In the range of low photon energy, the optical absorption coefficient ($\alpha(E)$) of disordered organic semiconductors obeys the Urbach rule: $\alpha(E) = \alpha_0 e^{(E-E_g)/E_U}$, where α_0 represents the optical absorption coefficient at the band edge, E is the photon energy, E_U is the Urbach energy,[64] which is usually described as the width of the tail of the DOS and a measure of energetic disorder.[33] Note that a smaller Urbach energy generally suggests a smaller degree of energy disorder. As shown in Fig. 5d, the blend films of **PM6:Spiro-F** showed a smaller Urbach energy of 32.89 meV than that of 35.16 meV for **PM6:F-2F**, which could be also suggested by the slightly sharper absorption onset (Fig. 2b) and enlarged CCL (Table 3) relative to those of **PM6:F-2F** blend.[39] Obviously, the ordered molecular stacking in **PM6:Spiro-F** blend caused by the introduction of rigid spirocyclic alkyl chain, should account for the smaller energetic disorder and thus migrate the recombination loss of OSCs.

Conclusions

To summarize, rigidifying backbones of NFAs through the constraint of vibrational–rotational motion of highly flexible aliphatic side chains could lead a smaller energy loss. Based on

a typical NFA of **F-2F**, a rigid spirocyclic alkyl side chain is applied in NFAs for the first time to replace the two highly flexible n-octyl chains on fluorene unit, affording an optimal molecular packing with enhanced intermolecular actions and lower energetic disorders for **Spiro-F**. As a result, the OSC based on as cast **PM6:Spiro-F** blended film achieves a significantly higher PCE of 13.56% and much reduced recombination loss comparing to that of the control device of **F-2F**. This work demonstrated an effective strategy to reduce the energy loss and even improve the PCE of OSCs through the rigid spirocyclic alkyl side chain. Moreover, we believe this strategy could be applied for other efficient systems with much smaller bandgaps, though the molecule design might be challenging.

Conflicts of interest

The authors declare no conflict of interest.

Acknowledgements

Notes and references

1 J. S. Wu, S. W. Cheng, Y. J. Cheng and C. S. Hsu, *Chem. Soc. Rev.*, 2015, **44**, 1113–1154.

2 Z. Li, G. He, X. Wan, Y. Liu, J. Zhou, G. Long, Y. Zuo, M. Zhang and Y. Chen, *Adv. Energy Mater.*, 2012, **2**, 74–77.

3 G. Yu, J. Gao, J. C. Hummelen, F. Wudl and A. J. Heeger, *Science*, 1995, **270**, 1789–1791.

4 X. Wan, C. Li, M. Zhang and Y. Chen, *Chem. Soc. Rev.*, 2020, **49**, 2828–2842.

5 Y. Cui, Y. Xu, H. Yao, P. Bi, L. Hong, J. Zhang, Y. Zu, T. Zhang, J. Qin, J. Ren, Z. Chen, C. He, X. Hao, Z. Wei and J. Hou, *Adv. Mater.*, 2021, **33**, e2102420.

6 J. Yuan, Y. Zhang, L. Zhou, G. Zhang, H.-L. Yip, T.-K. Lau, X. Lu, C. Zhu, H. Peng, P. A. Johnson, M. Leclerc, Y. Cao, J. Ulanski, Y. Li and Y. Zou, *Joule*, 2019, **3**, 1140–1151.

7 Y. Cai, Y. Li, R. Wang, H. Wu, Z. Chen, J. Zhang, Z. Ma, X. Hao, Y. Zhao, C. Zhang, F. Huang and Y. Sun, *Adv. Mater.*, 2021, **33**, e2101733.

8 S. Bao, H. Yang, H. Fan, J. Zhang, Z. Wei, C. Cui and Y. Li, *Adv. Mater.*, 2021, **33**, e2105301.

9 J. Zhang, F. Bai, I. Angunawela, X. Xu, S. Luo, C. Li, G. Chai, H. Yu, Y. Chen, H. Hu, Z. Ma, H. Ade and H. Yan, *Adv. Energy Mater.*, 2021, **11**, 2102596.

10 Y. Pan, X. Zheng, J. Guo, Z. Chen, S. Li, C. He, S. Ye, X. Xia, S. Wang, X. Lu, H. Zhu, J. Min, L. Zuo, M. Shi and H. Chen, *Adv. Funct. Mater.*, 2021, DOI: 10.1002/adfm.202108614.

11 Z. Zheng, J. Wang, P. Bi, J. Ren, Y. Wang, Y. Yang, X. Liu, S. Zhang and J. Hou, *Joule*, 2021, **6**, 171–184.

12 J. Liu, S. Chen, D. Qian, B. Gautam, G. Yang, J. Zhao, J. Bergqvist, F. Zhang, W. Ma, H. Ade, O. Inganäs, K. Gundogdu, F. Gao and H. Yan, *Nat. Energy*, 2016, **1**, 16089.

13 S. M. Menke, N. A. Ran, G. C. Bazan and R. H. Friend, *Joule*, 2018, **2**, 25–35.

14 K. Yoshikawa, H. Kawasaki, W. Yoshida, T. Irie, K. Konishi, K. Nakano, T. Uto, D. Adachi, M. Kanematsu, H. Uzu and K. Yamamoto, *Nat. Energy*, 2017, **2**, 17032.

15 Z. Liu, L. Krückemeier, B. Krogmeier, B. Klingebiel, J. A. Márquez, S. Levcenko, S. Öz, S. Mathur, U. Rau, T. Unold and T. Kirchartz, *ACS Energy Lett.*, 2018, **4**, 110–117.

16 P. Cheng, G. Li, X. Zhan and Y. Yang, *Nat. Photonics*, 2018, **12**, 131–142.

17 M. Gruber, J. Wagner, K. Klein, U. Hörmann, A. Opitz, M. Stutzmann and W. Brütting, *Adv. Energy Mater.*, 2012, **2**, 1100–1108.

18 L. Meng, Y. Zhang, X. Wan, C. Li, X. Zhang, Y. Wang, X. Ke, Z. Xiao, L. Ding, R. Xia, H. L. Yip, Y. Cao and Y. Chen, *Science*, 2018, **361**, 1094–1098.

19 J. Benduhn, K. Tvingstedt, F. Piersimoni, S. Ullbrich, Y. Fan, M. Tropiano, K. A. McGarry, O. Zeika, M. K. Riede, C. J. Douglas, S. Barlow, S. R. Marder, D. Neher, D. Spoltore and K. Vandewal, *Nat. Energy*, 2017, **2**, 17053.

20 X.-K. Chen, D. Qian, Y. Wang, T. Kirchartz, W. Tress, H. Yao, J. Yuan, M. Hülsbeck, M. Zhang, Y. Zou, Y. Sun, Y. Li, J. Hou, O. Inganäs, V. Coropceanu, J.-L. Bredas and F. Gao, *Nat. Energy*, 2021, **6**, 799–806.

21 K. Vandewal, J. Benduhn, K. S. Schellhammer, T. Vangerven, J. E. Ruckert, F. Piersimoni, R. Scholz, O. Zeika, Y. Fan, S. Barlow, D. Neher, S. R. Marder, J. Manca, D. Spoltore, G. Cuniberti and F. Ortmann, *J. Am. Chem. Soc.*, 2017, **139**, 1699–1704.

22 Q. Liu, S. Smeets, S. Mertens, Y. Xia, A. Valencia, J. D'Haen, W. Maes and K. Vandewal, *Joule*, 2021, **5**, 2365–2379.

23 M. Panhans, S. Hutsch, J. Benduhn, K. S. Schellhammer, V. C. Nikolis, T. Vangerven, K. Vandewal and F. Ortmann, *Nat. Commun.*, 2020, **11**, 1488.

24 X. K. Chen and J. L. Brédas, *Adv. Energy Mater.*, 2017, **8**, 1702227.

25 S. D. Collins, C. M. Proctor, N. A. Ran and T.-Q. Nguyen, *Adv. Energy Mater.*, 2016, **6**, 1501721.

26 G. Garcia-Belmonte, P. P. Boix, J. Bisquert, M. Lenes, H. J. Bolink, A. La Rosa, S. Filippone and N. Martín, *J. Phys. Chem. Lett.*, 2010, **1**, 2566–2571.

27 N. I. Craciun, J. Wildeman and P. W. Blom, *Phys. Rev. Lett.*, 2008, **100**, 056601.

28 G. Garcia-Belmonte and J. Bisquert, *Appl. Phys. Lett.*, 2010, **96**, 113301.

29 M. Kuik, L. J. Koster, G. A. Wetzelaer and P. W. Blom, *Phys. Rev. Lett.*, 2011, **107**, 256805.

30 Z. He, B. Xiao, F. Liu, H. Wu, Y. Yang, S. Xiao, C. Wang, T. P. Russell and Y. Cao, *Nat. Photonics*, 2015, **9**, 174–179.

31 S. Xie, Y. Xia, Z. Zheng, X. Zhang, J. Yuan, H. Zhou and Y. Zhang, *Adv. Funct. Mater.*, 2018, **28**, 1705659.

32 L. Zuo, S. B. Jo, S. Y. Li, Y. Meng, R. J. Stoddard, Y. Liu, F. Lin, X. Shi, F. Liu, H. W. Hillhouse, D. S. Ginger, H. Chen and A. K. Jen, *Nat. Nanotechnol.*, 2022, **17**, 53–60.

33 S. Liu, J. Yuan, W. Deng, M. Luo, Y. Xie, Q. Liang, Y. Zou, Z. He, H. Wu and Y. Cao, *Nat. Photonics*, 2020, **14**, 300–305.

34 W. Gao, Q. An, C. Zhong, Z. Luo, R. Ming, M. Zhang, Y. Zou, F. Liu, F. Zhang and C. Yang, *Chem. Sci.*, 2018, **9**, 8142–8149.

35 Q. An, W. Gao, F. Zhang, J. Wang, M. Zhang, K. Wu, X. Ma, Z. Hu, C. Jiao and C. Yang, *J. Mater. Chem. A*, 2018, **6**, 2468–2475.

36 S. Li, L. Ye, W. Zhao, S. Zhang, S. Mukherjee, H. Ade and J. Hou, *Adv. Mater.*, 2016, **28**, 9423–9429.

37 S. Dai, F. Zhao, Q. Zhang, T. K. Lau, T. Li, K. Liu, Q. Ling, C. Wang, X. Lu, W. You and X. Zhan, *J. Am. Chem. Soc.*, 2017, **139**, 1336–1343.

38 G. Chai, J. Zhang, M. Pan, Z. Wang, J. Yu, J. Liang, H. Yu, Y. Chen, A. Shang, X. Liu, F. Bai, R. Ma, Y. Chang, S. Luo, A. Zeng, H. Zhou, K. Chen, F. Gao, H. Ade and H. Yan, *ACS Energy Lett.*, 2020, **5**, 3415–3425.

39 Z. Zhang, Y. Li, G. Cai, Y. Zhang, X. Lu and Y. Lin, *J. Am. Chem. Soc.*, 2020, **142**, 18741–18745.

40 F. Lin, K. Jiang, W. Kaminsky, Z. Zhu and A. K. Jen, *J. Am. Chem. Soc.*, 2020, **142**, 15246–15251.

41 D. Luo, X. Lai, N. Zheng, C. Duan, Z. Wang, K. Wang and A. K. K. Kyaw, *Chem. Eng. J.*, 2021, **420**, 129768.

42 K. Jiang, Q. Wei, J. Y. L. Lai, Z. Peng, H. K. Kim, J. Yuan, L. Ye, H. Ade, Y. Zou and H. Yan, *Joule*, 2019, **3**, 3020–3033.

43 S. Dong, T. Jia, K. Zhang, J. Jing and F. Huang, *Joule*, 2020, **4**, 2004–2016.

44 C. Li, J. Zhou, J. Song, J. Xu, H. Zhang, X. Zhang, J. Guo, L. Zhu, D. Wei, G. Han, J. Min, Y. Zhang, Z. Xie, Y. Yi, H. Yan, F. Gao, F. Liu and Y. Sun, *Nat. Energy*, 2021, **6**, 605–613.

45 X. Ke, L. Meng, X. Wan, M. Li, Y. Sun, Z. Guo, S. Wu, H. Zhang, C. Li and Y. Chen, *J. Mater. Chem. A*, 2020, **8**, 9726–9732.

46 X. Li, S. Luo, H. Sun, H. H.-Y. Sung, H. Yu, T. Liu, Y. Xiao, F. Bai, M. Pan, X. Lu, I. D. Williams, X. Guo, Y. Li and H. Yan, *Energy Environ. Sci.*, 2021, **14**, 4555–4563.

47 D. Luo, L. Li, Y. Shi, J. Zhang, K. Wang, X. Guo and A. K. K. Kyaw, *J. Mater. Chem. A*, 2021, **9**, 14948–14957.

48 R. Steyrleuthner, M. Schubert, I. Howard, B. Klaumunzer, K. Schilling, Z. Chen, P. Saalfrank, F. Laquai, A. Facchetti and D. Neher, *J. Am. Chem. Soc.*, 2012, **134**, 18303–18317.

49 M. Zhang, X. Guo, W. Ma, H. Ade and J. Hou, *Adv. Mater.*, 2015, **27**, 4655–4660.

50 M. Schubert, D. Dolfen, J. Frisch, S. Roland, R. Steyrleuthner, B. Stiller, Z. Chen, U. Scherf, N. Koch, A. Facchetti and D. Neher, *Adv. Energy Mater.*, 2012, **2**, 369–380.

51 X. Gong, M. Tong, F. G. Brunetti, J. Seo, Y. Sun, D. Moses, F. Wudl and A. J. Heeger, *Adv. Mater.*, 2011, **23**, 2272–2277.

52 A. K. Kyaw, D. H. Wang, D. Wynands, J. Zhang, T. Q. Nguyen, G. C. Bazan and A. J. Heeger, *Nano Lett.*, 2013, **13**, 3796–3801.

53 M. M. Mandoc, F. B. Kooistra, J. C. Hummelen, B. de Boer and P. W. M. Blom, *Appl. Phys. Lett.*, 2007, **91**, 263505.

54 C. G. Shuttle, B. O'Regan, A. M. Ballantyne, J. Nelson, D. D. C. Bradley, J. de Mello and J. R. Durrant, *Appl. Phys. Lett.*, 2008, **92**, 093311.

55 D. Hu, Q. Yang, H. Chen, F. Wobben, V. M. Le Corre, R. Singh, T. Liu, R. Ma, H. Tang, L. J. A. Koster, T. Duan, H. Yan, Z. Kan, Z. Xiao and S. Lu, *Energy Environ. Sci.*, 2020, **13**, 2134–2141.

56 Y. Shen, A. R. Hosseini, M. H. Wong and G. G. Malliaras, *ChemPhysChem*, 2004, **5**, 16–25.

57 D. M. Smilgies, *J. Appl. Crystallogr.*, 2009, **42**, 1030–1034.

58 U. Rau, B. Blank, T. C. M. Müller and T. Kirchartz, *Phys. Rev. Appl.*, 2017, 7, 044016.

59 S. Chen, Y. Wang, L. Zhang, J. Zhao, Y. Chen, D. Zhu, H. Yao, G. Zhang, W. Ma, R. H. Friend, P. C. Y. Chow, F. Gao and H. Yan, *Adv. Mater.*, 2018, **30**, e1804215.

60 U. Rau, *Phys. Rev. B: Condens. Matter Mater. Phys.*, 2007, **76**, 085303.

61 T. Kirchartz and J. Nelson, *Phys. Rev. B: Condens. Matter Mater. Phys.*, 2012, **86**, 165201.

62 T. Kirchartz, B. E. Pieters, J. Kirkpatrick, U. Rau and J. Nelson, *Phys. Rev. B: Condens. Matter Mater. Phys.*, 2011, **83**, 115209.

63 J. Yao, T. Kirchartz, M. S. Vezie, M. A. Faist, W. Gong, Z. He, H. Wu, J. Troughton, T. Watson, D. Bryant and J. Nelson, *Phys. Rev. Appl.*, 2015, **4**, 014020.

64 F. Urbach, *Phys. Rev.*, 1953, **92**, 1324.